

Date of publication xxxx 00, 0000, date of current version xxxx 00, 0000.

Digital Object Identifier 10.1109/ACCESS.2017.Doi Number

Volume Conduction for Powering Deeply Implanted Networks of Wireless Injectable Medical Devices: a Numerical Parametric Analysis

MARC TUDELA-PI¹, JESUS MINGUILLON¹, LAURA BECERRA-FAJARDO¹, ANTONI IVORRA^{1,2}

¹Department of Information and Communications Technologies, Universitat Pompeu Fabra, 08018 Barcelona, Spain

²Serra Hùnter Fellow Programme, Universitat Pompeu Fabra, 08018 Barcelona, Spain

Corresponding author: Antoni Ivorra (antoni.ivorra@upf.edu).

This work was supported by the European Research Council (ERC) under the European Union's Horizon 2020 Research and Innovation Programme under Grant 724244. The work of Antoni Ivorra was supported by the ICREA under the ICREA Academia Programme.

ABSTRACT The use of networks of wireless active implantable medical devices (AIMDs) could revolutionize the way that numerous severe illnesses are treated. However, the development of sub-mm AIMDs is hindered by the bulkiness and the transmission range that consolidated wireless power transfer (WPT) methods exhibit. The aim of this work is to numerically study and illustrate the potential of an innovative WPT technique based on volume conduction at high frequencies for powering AIMDs. In this technique, high frequency currents are coupled into the tissues through external electrodes, producing an electric field that can be partially picked-up by thin, flexible, and elongated implants. In the present study, the system formed by the external electrodes, the tissues and the implants was modeled as a two-port impedance network. The parameters of this model were obtained using a numerical solver based on the finite element method (fem). The model was used to determine the power delivered to the implants' load (PDL) and the power transmission efficiency (PTE) of the system. The results allow the identification of the main features that influence the PDL and the PTE in a volume conduction scenario and demonstrate that volume conduction at high frequencies can be the basis for a non-focalized WPT method that can transfer powers above milliwatts to multiple mm-sized implants ($< 10 \text{ mm}^3$) placed several centimeters ($> 3 \text{ cm}$) inside the tissues.

INDEX TERMS volume conduction, active implants, wireless power transmission, WPT, finite element analysis, numerical models, fem

I. INTRODUCTION

The use of active implantable medical devices (AIMDs) has the potential to revolutionize the health industry for years to come [1], [2]. In particular, the development of dense networks of miniaturized (mm-sized or less), minimally invasive and distributed AIMDs that allow for efficient interaction with the nervous system could drastically change the way that several major diseases are approached (e.g., tetraplegia, tremor suppression) [3]–[5], and facilitate the development of next generation wearable robots [6]. However, miniaturization, and thus the development of these envisioned swarms of networked AIMDs, has been hampered by the way implantable electronic devices are

powered. On the one hand, current batteries have limited power density for allowing the implementation of mm-sized devices that can operate for long periods of time. On the other hand, several wireless power transfer (WPT) methods have been developed for supplying power to battery-less AIMDs but, to the best of our knowledge, in all cases require relatively bulky components within the implants for receiving the energy transferred by the remote transmitter. Inductive and ultrasonic coupling are the two most widely used WPT methods [7]. Both methods are useful to transfer powers in the order of mW to a single AIMD [8]–[13], but they present several limitations for distributed networks of AIMDs.

In the case of inductive coupling, the power delivered to the implant load (PDL) and power transmission efficiency (PTE) notably decrease as the separation between the transmitter and the receiver coils increases, as well as with misalignments between them [14]. Recently, to minimize these losses, some authors have proposed the use of a third coil located between the transmitter and the receiver [9], [15]. In particular, this approach has been used for powering a distributed network of mm-sized implants for brain-computer interface applications [16]. However, the cm-sized intermediate coil was also implanted, thus creating a more invasive system. It is difficult to conceive the use of this approach in soft tissue regions such as the limbs or the abdomen, as this additional coil would be excessively stiff and bulky.

Ultrasonic WPT can deliver powers in the order of mW to implants located several centimeters inside the tissues when the ultrasonic waves are focused on a specific region [17]. However, there is a trade-off between the received power and the spatial range; high power will be obtained by focusing the beam, while low power will be obtained if the beam is spread. This reduces the applicability of ultrasounds for powering networks of distributed AIMDs.

In the last years, we have explored the use of volume conduction to power networks of implants [18]–[21]. The WPT technique proposed does not require embedding bulky components inside the implants to electrically power them. The technique consists in the delivery of bursts of high-frequency currents through pairs of external textile electrodes and the development of thread-like devices, which can be deeply implanted by minimally invasive procedures. The electric currents, due to the conductive properties of the tissues, produce a voltage gradient that can be picked up by thin (< 1 mm) and elongated (~ 3 cm) implants. The implants draw power from the high-frequency current bursts through electronic rectification. The rectifier, together with the supplied electronics can be integrated into a microcircuit or an application-specific integrated circuit (ASIC). This implies that the implants can be shaped as thin and flexible devices that can be deployed by injection or catheterization [22]. Fig. 1a illustrates an envisioned scenario, where multiple thread-like AIMDs are placed in the muscle of an upper arm, and the electric field is applied by two external electrodes made of conductive fabric.

In [18] we demonstrated that injectable stimulators based on off-the-shelf components could be powered and addressed from an external unit. In [19], we proposed a two-port network to model the whole system for circuit simulation. Recently, we have developed an analytical model able to determine the maximum power that an implant can locally obtain considering an infinite homogeneous medium [20]. We have also conducted an experimental study in humans demonstrating the feasibility of this WPT technique (preprint [21]). However, to the best of our knowledge,

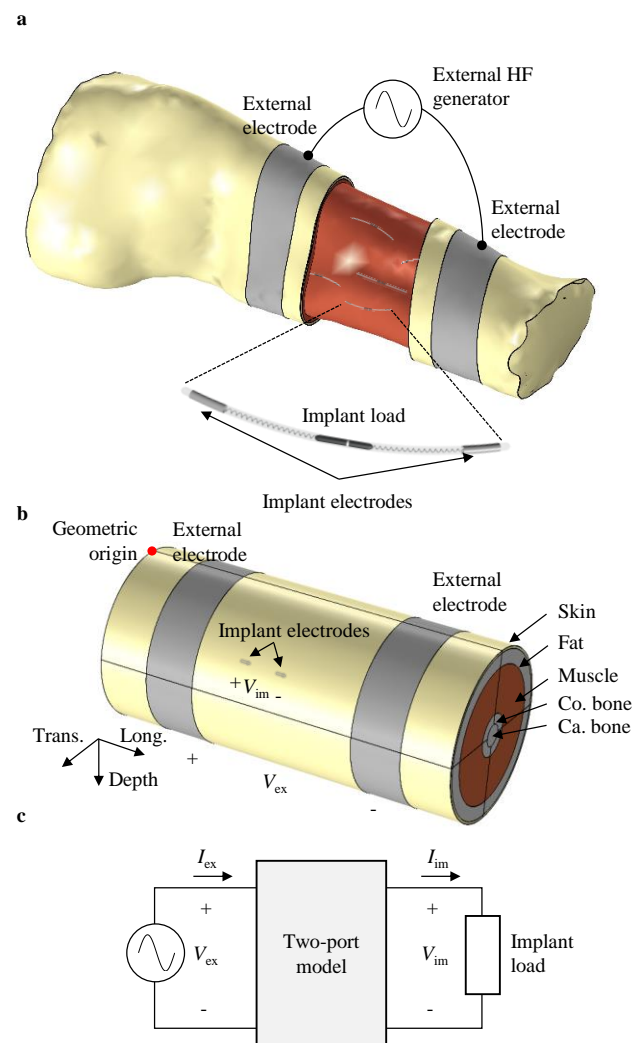


FIGURE 1. a) Envisioned scenario where a swarm of thread-like AIMDs are powered using volume conduction. **b)** Simplified model of an upper arm that consists in a multilayered concentric cylinder (skin, fat, muscle, cortical bone, and cancellous bone), two external electrodes and two cylindrical electrodes that emulate an implant. **c)** Two-port network model of the coupling between the external electronic system and the implant electronics.

the complete transmission link (i.e., the combination of external electrodes, multilayered tissue, and implants) for the described technique has not been studied in detail yet. For this reason, the present work aims to numerically study the volume conduction transmission link and its potential for powering networks of deeply implanted AIMDs in human limbs. In particular, this work is a parametric analysis in which the dependence on several geometrical and anatomical parameters is analyzed. Unlike the local model presented in [20], here it is considered a more realistic scenario that includes the whole transmission link (Fig. 1b). Additionally, the system is modeled using a two-port network (Fig. 1c) instead of using an analytical approach, since an interpretable closed analytical expression is not feasible because the medium is finite and includes multiple tissue

layers. The parameters of the two-port network were obtained using a finite element method (fem) solver. In order to parametrically analyze how different geometrical and anatomical parameters influence the PDL and the PTE, the limb was simplified using a concentric cylindrical approach as it has been done in previous studies in which volume conduction has been analyzed for communications [23]–[25].

II. BACKGROUND: VOLUME CONDUCTION AND ELECTRICAL SAFETY

International safety standards [26], [27] identify two main sources of risk with respect to human exposure to radio frequency electromagnetic fields: neuromuscular stimulation and tissue heating. The risk of stimulation is directly related to the electric field, E (V_{rms}/m), and the frequency applied, being especially relevant for frequencies below 100 kHz. In particular, the IEEE safety standard [26] considers that for continuous sinusoidal waveforms at frequencies above 5 MHz the risk of electrostimulation is negligible. Regarding tissue heating due to Joule's effect, the standards define a maximum specific absorption rate (SAR) to avoid tissue overheating. The SAR is expressed in W/kg and can be calculated at any point as

$$\text{SAR} = \frac{\sigma |E_{\text{rms}}|^2}{\rho}, \quad (1)$$

where σ is the tissue conductivity (S/m), and ρ is the tissue density (kg/m³). The SAR is averaged over 10 g of tissue for 6 minutes. The safety standards establish a limit of 20 W/kg for human extremities in controlled environments [26], [27].

In this work, the electrostimulation risk is not addressed as we propose the use of currents with a frequency of 6.78 MHz, which is above the 5 MHz limit. The 6.78 MHz corresponds to the central frequency of an ISM radio band, thus the possibility of interfering radiocommunications is minimized. We advise against the use of higher ISM radio bands (above 10 MHz) to avoid losses due to skin effect, as at those frequencies the skin effect may be very substantial [28], especially in cases where the AIMDs are implanted several centimeters into the tissues.

III. MODELLING

The volume conduction links formed by the external electrodes, the upper arm tissues and the implants' electrodes were modeled using multi-port networks. The impedance parameters of these networks were obtained using a fem solver.

A. GEOMETRY

The upper arm geometry was simplified as a five-layer concentric cylinder, as shown in Fig. 2a-b, where each layer emulates a tissue: dry skin, fat, muscle, cortical bone, and cancellous bone (Fig. 2). Table I reports the thicknesses

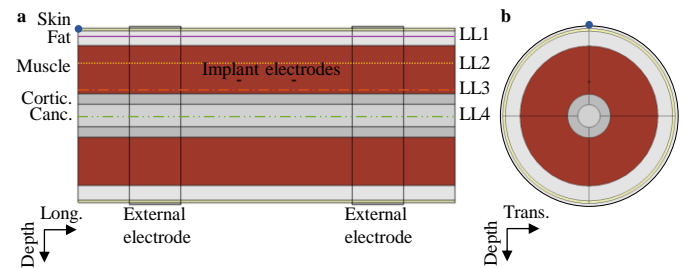


FIGURE 2. Schematic views of the model. The implant electrodes (plotted in black) are placed at a depth of 30 mm and longitudinally aligned with the multilayered cylinder. a) Longitudinal mid cross section. Longitudinal lines LL1, LL2, LL3, and LL4 are located in fat (depth = 5 mm), muscle (depth = 20 mm), muscle (depth = 35 mm) and cancellous bone (depth = 50 mm) respectively. b) Transverse mid cross section.

TABLE I
MODEL NOMINAL DIMENSIONS

Description	Value (mm)
Limb segment (multilayered cylinder)	
Length	220
Dry skin thickness	1.5
Fat thickness	8.5
Muscle thickness	27.5
Cortical bone thickness	6
Cancellous bone thickness	6.5
External electrodes	
Length	30
Inner radius	50
Electrode thickness	1
Implant electrodes	
Length	2
Diameter	0.5
Separation distance	30

TABLE II
ELECTRICAL PROPERTIES AND DENSITY OF THE MATERIALS

Tissue/Material	Conductivity σ (S/m)	Relative permittivity ϵ_r	Density ρ (kg/m ³)
Dry skin	0.15	478	1109
Fat	0.03	16	911
Muscle	0.60	233	1090
Cortical bone	0.04	48	1908
Cancellous bone	0.12	90	1178
Stainless steel	$1.4 \cdot 10^6$	1	8000

used for each layer. Similar models have been broadly used to model the upper arm in galvanic coupling communication models [23], [25], [29]. Since all the tissues can be considered electrically isotropic for high frequencies [30], and the quasi-electrostatic condition is considered, each layer was simply electrically characterized with two scalars: conductivity (σ) and permittivity (ϵ). The electrical values of these parameters, for a frequency of 6.78 MHz, were taken from [31], while the tissue density was obtained from [32]. These parameters are reported in Table II.

Although we have proposed and demonstrated the use of external electrodes made of conductive fabric that could be embedded in garments [18], in this simplified model the

external electrodes consisted in a pair of cylindrical rings embracing the skin with dielectric properties and density equivalent to those of stainless steel [33]. Their dimensions are also reported in Table I. Unless otherwise indicated, the separation distance between the edges of both electrodes was 100 mm and their length was 30 mm.

Regarding the elongated implant, for the sake of simplicity, it was modeled as an aligned pair of stainless-steel cylindrical electrodes separated at a given distance. Their dimensions are reported in Table I. Unless otherwise stated, the implant electrodes were placed at a depth of 30 mm. They were longitudinally aligned with the multilayered cylinder, placing one electrode at the longitude of 95 mm and the other one at 135 mm. For both electrodes, the transverse position was set to zero (see Fig. 2a-b).

B. MULTI-PORT NETWORK MODEL

The system composed of the external electrodes, the tissues, and the implants' electrodes, is linear and reciprocal for low current densities [34]. For this reason, it can be modeled with a multi-port network. For the case of a single implant, the system can be modeled as a two-port network [35]

$$\begin{bmatrix} V_{ex} \\ V_{im} \end{bmatrix} = \begin{bmatrix} Z_{ex} & Z_{exim} \\ Z_{exim} & Z_{im} \end{bmatrix} \begin{bmatrix} I_{ex} \\ I_{im} \end{bmatrix}, \quad (2)$$

where V_{ex} (V_{rms}) and I_{ex} (A_{rms}) are the transmitter voltage and current phasors, while V_{im} (V_{rms}) and I_{im} (A_{rms}) are the implant voltage and current phasors, and the impedances are defined as

$$Z_{ex} \stackrel{\text{def}}{=} \frac{V_{ex}}{I_{ex}} \Big|_{I_{im}=0}, Z_{im} \stackrel{\text{def}}{=} \frac{V_{im}}{I_{im}} \Big|_{I_{ex}=0}, Z_{exim} \stackrel{\text{def}}{=} \frac{V_{ex}}{I_{im}} \Big|_{I_{ex}=0}, \quad (3)$$

where Z_{ex} corresponds to the impedance between the two external electrodes, Z_{im} is the impedance between the implant electrodes, and Z_{exim} is the transimpedance between the external electrodes and the implant electrodes. For the studied frequency, the tissue impedance seen by the implant electrodes is mostly resistive due to the biological properties of the tissues (see Table II). Assuming a purely resistive Z_{im} , the maximum power is transferred to the load when the implant load (R_L) matches Z_{im} . For this reason, R_L was set to be equal to the real part of Z_{im} . Consequently, the implant current was defined as

$$I_{im} = -\frac{V_{im}}{R_L}. \quad (4)$$

For the cases in which two implants were considered, the two-port model (2) was expanded to a multiport model

$$\begin{bmatrix} V_{ex} \\ V_{im1} \\ V_{im2} \end{bmatrix} = \begin{bmatrix} Z_{ex} & Z_{exim1} & Z_{exim2} \\ Z_{exim1} & Z_{im1} & Z_{im1im2} \\ Z_{exim2} & Z_{im1im2} & Z_{im2} \end{bmatrix} \begin{bmatrix} I_{ex} \\ I_{im1} \\ I_{im2} \end{bmatrix}, \quad (5)$$

where

$$Z_{im1im2} \stackrel{\text{def}}{=} \frac{V_{im2}}{I_{im1}} \Big|_{I_{im2}=0, I_{ex}=0}. \quad (6)$$

C. EXTRACTION OF PARAMETERS FOR THE MULTI-PORT NETWORK

For the described scenario, the quasi-static electric field approach can be assumed, since for a frequency of 6.78 MHz, the electric field wavelength is much larger than the model dimensions.

The model geometry described in Fig. 2 was implemented in COMSOL Multiphysics 5.3 (from COMSOL, Inc., Burlington, MA, US) to calculate the electric field distributions and the parameters of the multi-port network model using the "Electric Currents (ec)" physics from the "AC/DC module". This physics mode considers the quasistatic approach and solves the following equations

$$\nabla \cdot \mathbf{J} = -\frac{\partial \rho_c}{\partial t}, \quad (7)$$

where \mathbf{J} is the current density (A/m^2) and ρ_c is the charge density (C/m^3),

$$\mathbf{J} = \sigma \mathbf{E} + i\omega \mathbf{D}, \quad (8)$$

being ω the angular frequency of the field (rad/s), and \mathbf{D} the electric displacement field (C/m^2),

$$\mathbf{D} = \epsilon_0 \epsilon_r \mathbf{E}. \quad (9)$$

And

$$\mathbf{E} = -\nabla V_{rms}. \quad (10)$$

The used mesh consisted of two tetrahedral meshes. The first one was applied in the regions close to the implant electrodes (< 5 mm from their centers), imposing a maximum edge length of 0.1 mm. This refined mesh was used to obtain a proper resolution and therefore accurate impedance values for the implant electrodes. The second one comprises the rest of the geometry and was automatically generated. The total number of elements was comprised between 1,000,000 and 1,200,000.

The multi-port impedance parameters were extracted simulating the delivery of a known current ($f = 6.78$ MHz) through the selected electrodes and measuring the received voltage at the electrodes of interest, see (3). To calculate the averaged SAR, the normalized values of the simulated \mathbf{E}_{rms} and σ were stored in a regular 3-D grid (steps of 1 mm) for the whole geometry. Then, using MATLAB R2019a (from MathWorks, Inc., Natick, MA, US), the local SAR (1) was averaged over cubes with a volume of ~ 10 cm³ (edge equal to 21 mm and an approximately mass of 10 g) for each of the grid points. The peripheral points that could not be the center of a cube, as the cube included points outside the tissues, were assigned to the highest spatial-average in which they were enclosed as indicated by the IEC/IEEE 62704-1 standard [36].

D. POWER DELIVERED TO THE IMPLANT AND POWER TRANSFER EFFICIENCY

The PDL can be calculated as

$$PDL = \frac{|V_{im}|^2}{R_L}. \quad (11)$$

The active power (P_{in}) coupled to the tissues by the external electrodes is calculated as

$$P_{in} = I_{ex} V_{ex} \cos(\varphi), \quad (12)$$

where φ is the phase (rad) between V_{ex} and I_{ex} . As most of the power is dissipated at the tissues and only a tiny portion can be dissipated at the implants, the applied power (12) can be approximated as

$$P_{in} \approx I_{ex}^2 \Re(Z_{ex}). \quad (13)$$

Therefore, the PTE is calculated as

$$PTE = \frac{\sum_{m=1}^N PDL_m}{P_{in}}, \quad (14)$$

where N is the total number of implants.

IV. RESULTS

A. ELECTRIC FIELD INSIDE THE TISSUES

The amplitude of the external high frequency current that can be coupled to the tissues is limited by the SAR restrictions. For the nominal model of Table I, it was found that the applied current must be below $0.46 A_{rms}$ (at 6.78 MHz), since above this value, the local averaged SAR will exceed the 20 W/kg limit. If not otherwise indicated, this will be the applied current for the following cases. Fig. 3 shows the averaged SAR distribution when the external electrodes apply $0.46 A_{rms}$ at 6.78 MHz. The results highlight that the averaged SAR is focused close to the external electrodes and has a maximum value of 20 W/kg.

Fig. 4a shows the electric field distribution along four longitudinal lines at the depths of 5 mm, 20 mm, 35 mm, and 50 mm (see Fig. 2a). The maximum electric field is located close to both external electrodes (see LL1, which runs through the middle of the fat layer). However, it can be observed how the electric field tends to be uniform a few centimeters away from the external electrodes. Considering the most central segment of the model (i.e., longitudes between 95 mm and 125 mm) the electric field can be considered depth-independent (e.g., at a depth of 50 mm the electric field is just 1.5% lower than at a depth of 5 mm, for the entire range). The electric field at the midpoint between the external electrodes (i.e., longitude position equal to 110 mm) is about $155 V_{rms}/m$. Considering an implant with a length of 30 mm and aligned parallel to the applied electric field, the voltage that this implant can pick up is $4.65 V_{rms}$ (see Fig. 4b). It is worth noting that, although this will be the maximum rms amplitude because of the SAR limitation, it will be possible to obtain much higher peak amplitudes by delivering the ac currents in the form of short bursts [20], [21].

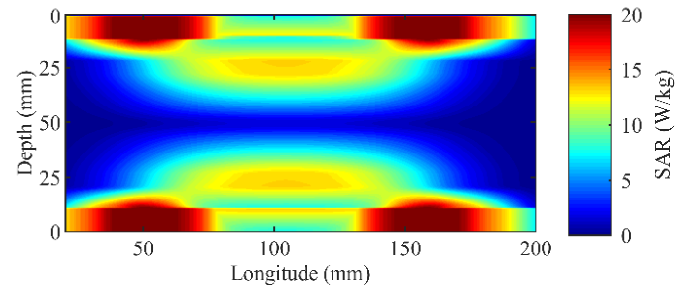


FIGURE 3. Distribution of the SAR averaged over a 10 g cube (longitudinal mid cross section). The current applied between both external electrodes was $0.46 A_{rms}$. The maximum SAR was located close to both external electrodes (20 W/kg).

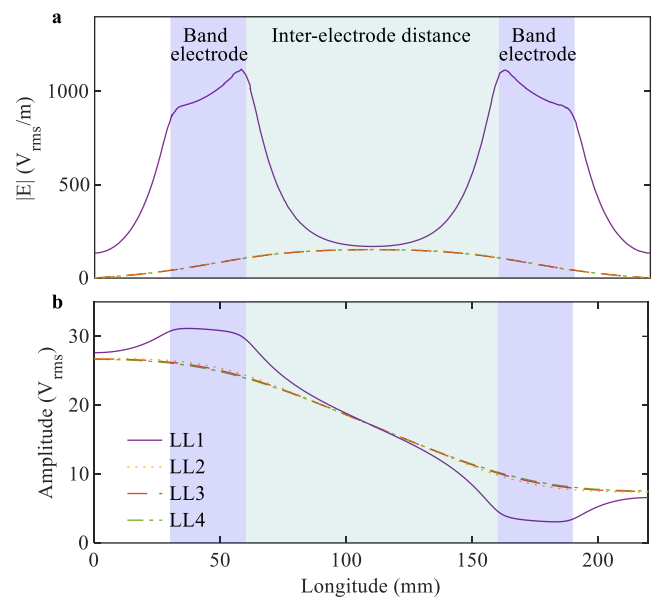


FIGURE 4. a) Electric field (rms) and b) rms voltage distribution along four longitudinal lines (see Fig. 2a). LL1: depth = 5 mm (fat), LL2: depth = 20 mm (muscle), LL3: depth = 35 mm (muscle), and LL4: depth = 50 mm (cancellous bone).

B. IMPLANTATION DEPTH

To study the PDL and PTE as a function of the implantation depth, the longitudinal position of the implant electrodes was set to 95 mm and 125 mm respectively while the transverse position was zero for both electrodes. The electrodes' depth was swept from the peripheral fat layer (depth = 3 mm) to the cancellous bone (depth = 50 mm), see Fig. 5.

The results show that the maximum PDL is obtained when the implant electrodes are surrounded by muscle tissue (PDL = 11.8 mW, PTE = 0.07%, and depth = 22 mm). The lowest PDL is obtained when the implant is surrounded by fat tissue (PDL = 0.4 mW, PTE = 0.004%, and depth = 7 mm). This difference in the PDL between different layers is mostly related to the tissue impedance seen by the implant electrodes. At a depth of 5 mm (i.e., fat tissue) the tissue impedance seen by the implant electrodes (Z_{im}) is $8612-1262i \Omega$, while for a depth of 25 mm (i.e., muscle tissue) is $464-50i \Omega$.

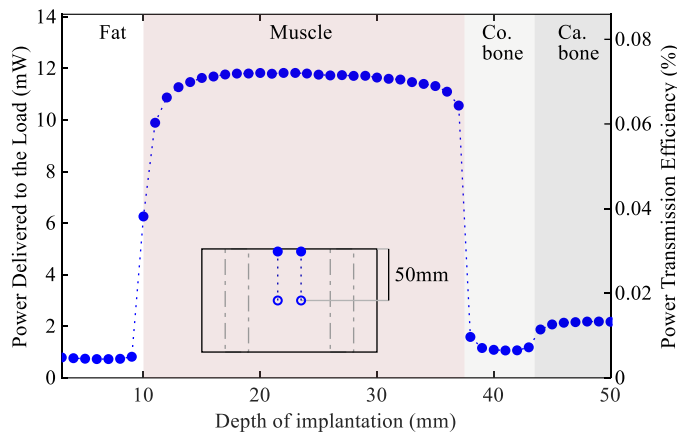


FIGURE 5. PDL and PTE as a function of the implantation depth. Co. bone: Cortical bone, Ca. bone: Cancellous bone. The inset shows the electrodes displacement. The displacement is illustrated in the supplementary material ("S5.gif").

As the maximum power is transferred to the load approximately when R_L matches the real part of Z_{im} , Z_{im} directly affects the obtained PDL (11). Nevertheless, the obtained PDL as a function of the depth is hardly affected by the maximum voltage that an implant can pick up since, for the studied area, the maximum voltage that an implant could receive is not related to its implantation depth (Fig. 2b).

C. EXTERNAL ELECTRODES SEPARATION

Fig. 6 illustrates the influence of the separation distance between the inner edges of the external electrodes. In this figure the separation distance between the external electrodes was symmetrically increased from 30 mm to 120 mm while the implant electrodes were kept at the default position (i.e., an implantation depth of 30 mm, a transverse position of 0 mm, and a longitudinal position of 95 mm and 135 mm for the first and second electrode respectively). The amplitude of the applied current was adjusted to obtain a SAR of 20 W/kg, resulting in a current amplitude of 0.46 A_{rms} for the entire range studied. The results show that the PDL is reduced when the external electrodes are aligned over the implant electrodes (i.e., a separation distance of 30 mm regarding the depth axis), as the electric field E is focused on the more superficial layers (see Fig. 4a). In this case, the implant picked up 2.8 mW with a PTE of 0.03%. PDL increases with the separation distance of the external electrodes. The maximum power transferred is for the case where the external electrodes were separated 120 mm. For this case, the PDL is 11.6 mW and the PTE is 0.068%. PTE has its maximum (0.072%) for a separation of 90 mm.

D. EXTERNAL ELECTRODES WIDTH

To determine the influence of the width of the external electrodes, their size was swept from 10 mm to 35 mm (Fig. 7) while the separation distance between the edges of

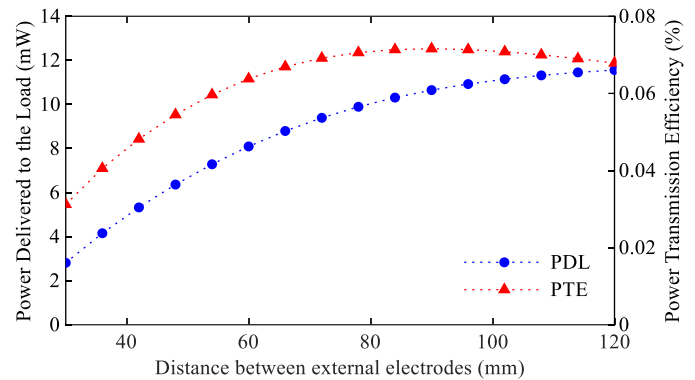


FIGURE 6. PDL and PTE as a function of the separation distance between edges of the external electrodes. The displacement is illustrated in the supplementary material ("S6.gif").

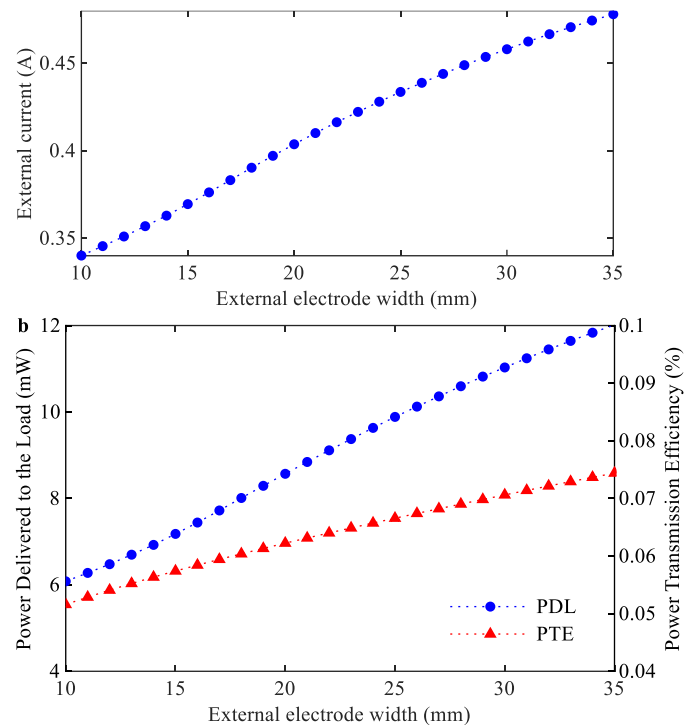


FIGURE 7. a) Admissible external current to produce a maximum averaged SAR of 20 W/kg. b) PDL and PTE as a function of the external electrode width. The electrode width increment is illustrated in the supplementary material ("S7.gif").

the electrodes was kept constant at 100 mm. The current applied for each band size was set to obtain a maximum averaged SAR of 20 W/kg (Fig. 7a) ranging from 0.345 A_{rms} to 0.49 A_{rms}. The results show that as the band electrodes get wider, the PDL and PTE obtained are also higher (Fig. 7b).

E. FAT THICKNESS

One of the anatomical parameters of the model that varies more between individuals is the fat thickness [37]. To study how the fat thickness can influence in the PDL and the PTE, the thickness of this layer was swept from 1 mm to 25 mm, while the thicknesses of the dry skin, cancellous bone and cortical bone were kept constant, and the muscle thickness

was modified to obtain a total radius of 50 mm (i.e., the limb radius was kept constant to allow the comparison between cases). Again, the external current I_{ex} was set to obtain a maximum averaged SAR of 20 W/kg (Fig. 8a) ranging from 0.34 A_{rms} to 0.69 A_{rms} . The results indicate that to avoid tissue over-heating, the applied I_{ex} must be reduced as the fat thickness is increased (Fig. 8a). Interestingly, the results show that as the fat layer gets thicker, the power that an implant placed in the muscle can obtain is higher (Fig. 8b). The minimum PDL value corresponds to a 5 mm fat layer (PDL = 10.6 mW, and PTE = 0.067%).

F. INTERACTION OF MULTIPLE IMPLANTS

To determine how neighboring implants may influence the PDL of each individual implant, a parametric sub-analysis was performed varying the separation distance of two parallel implants along two different axes independently. In this sub-analysis it was assumed a minimum separation distance of 3 mm between both parallel devices due to implantation limitations. In this sub-analysis it was also assumed that the load of both implants corresponds to the real part of Z_{im} .

In Fig. 9a a longitudinal displacement was done while fixing the length of both implants to 30 mm. The position of *Implant 1* was kept constant, while *Implant 2* was longitudinally displaced along an axis 3 mm more superficial. The longitudinal position of the left electrode of *Implant 2* was swept from 45 mm to 145 mm. During this displacement, the implantation depth of both electrodes of *Implant 2* was kept constant at 27 mm and their transverse position was 0 mm (see inlet Fig. 9a or “S9a.gif”).

In the second case, the displacement was done with respect to the implantation depth (Fig. 9b). Here, the location of *Implant 1* was kept constant at a depth of 30 mm, while the depth position of *Implant 2* was swept from 3 mm to 27 mm (i.e. 3 mm away from *Implant 1*), keeping the transverse position equal to zero, and both electrodes aligned parallel to the electrodes of *Implant 1* regarding the longitudinal axis (see inlet in Fig. 9b or “S9b.gif”).

Fig. 9 shows that the PDL moderately decreases for both implants as the separation distance between electrodes is reduced. For instance, the PDL obtained by *Implant 1* when the electrodes of both implants are placed parallel at a depth separation of 3 mm is 9.5 mW (i.e., a reduction of 19.5% compared to the single implant case, see Fig. 5b). However, this power reduction becomes less than 10% for depth separations above 10.5 mm. When two electrodes of different implants are placed consecutively on the longitudinal axis (e.g., a longitudinal separation of ± 30 mm regarding the left electrodes, and a depth separation of 3 mm, see Fig. 9a) the obtained power is also reduced.

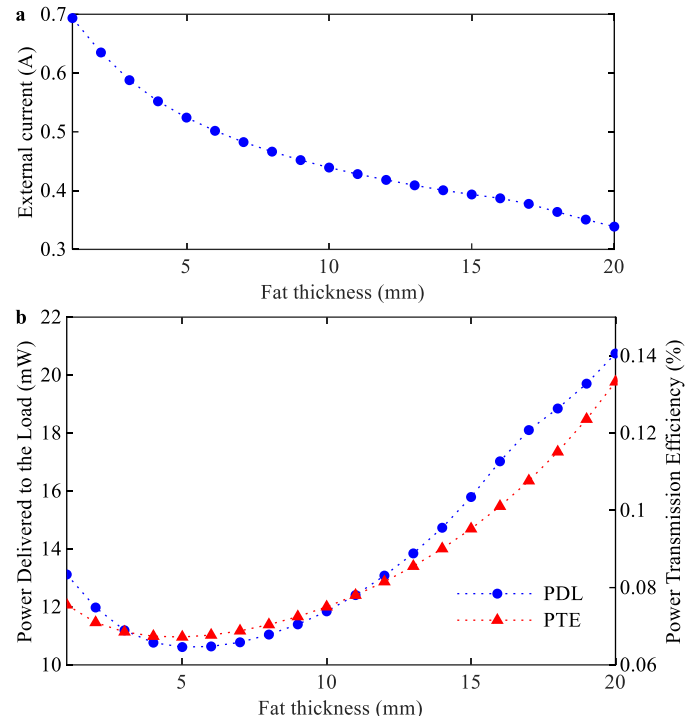


FIGURE 8. a) Admissible external current to produce a maximum averaged SAR of 20 W/kg. **b)** PDL and PTE as a function of the fat layer thickness imposing a SAR of 20 W/kg. The fat thickness increment is illustrated in the supplementary material (“S8.gif”).

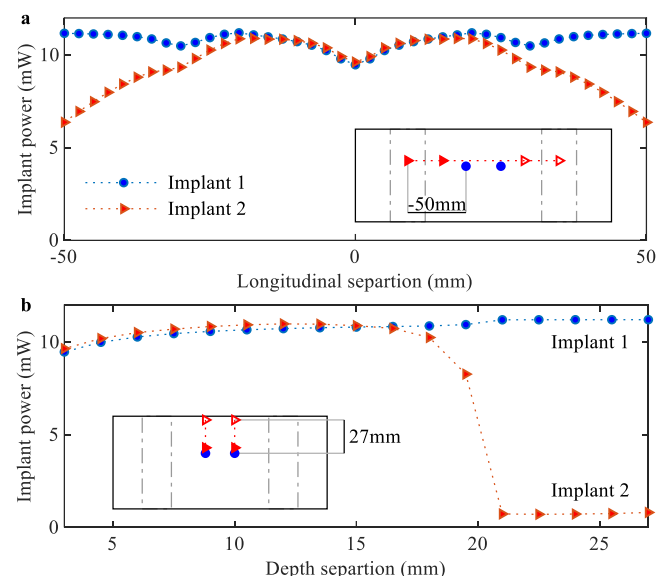


FIGURE 9. PDL as a function of the distance between two 30 mm length implants. a) Longitudinal displacement. Regarding the left electrodes of both implants the longitudinal displacement was from -50 mm to +50 mm (see inlet Fig. 9a). **b)** Displacement regarding the depth position. Both implants were parallel aligned regarding the longitudinal axis. The displacement between implants was from 3 mm to 27 mm regarding the depth axis (see inlet Fig. 9b). The displacements are illustrated in the supplementary material (“S9a.gif”, and “S9b.gif”).

In this case, the PDL is reduced 11% compared to the single implant case (Fig. 5b). The substantial reduction in PDL observed in Fig. 9a for large longitudinal separations and in Fig. 9b for large depth separations is not due to the

interaction between the implants, but to the non-uniformity of the electric field and to the change of tissue type respectively.

G. FIBROUS CAPSULE AROUND THE IMPLANT

The presence of an artificial implant within the human body will trigger physiological reactions that will end up producing a fibrous tissue capsule around the device, even if the implanted device is considered to be biocompatible [38]. In the systems considered here, this encapsulation will modify the tissue impedance seen by the implants, and therefore the PDL. The two main factors that will contribute to the impedance change will be the capsule conductivity and the capsule thickness.

A sub-analysis was conducted to study the potential impact of the encapsulation. The conductivity of the fibrous tissue can be considered mostly frequency independent, with a conductivity of 0.16 ± 0.1 S/m for a fibrotic capsule formed around silicone rubber [39]. Thus, here a fibrotic conductivity of 0.16 S/m was assumed. The implant electrodes were positioned at the default location of Table I, within muscle tissue. The modeled thicknesses of the fibrotic capsule ranged from 0.1 to 1 mm.

Fig. 10 shows that, for the described scenario, a capsule of just 0.1 mm substantially reduces the maximum power that the implant could pick up; the PDL drops from 11.6 mW (Fig. 5) to 6.6 mW. Interestingly, the rate of PDL drop decreases with the thickness and for a tenfold thickness, 1 mm, the PDL is still considerably high (3.7 mW).

H. IMPLANT ELECTRODE SIZE

The size of the implant electrodes has a direct effect on the impedance across them (i.e., Z_{im}) [20]. To study their contribution to the PDL and PTE, the length of the implant electrodes was changed from 1 mm to 3.5 mm for two different electrode diameters (0.5 mm and 0.25 mm), while the separation distance between electrodes was kept constant. The results show that for the studied range, the PTE depends linearly on the PDL, and confirm that as in [20] the power is maximized by increasing the size of the implant electrodes (Fig. 11).

I. RADIUS OF THE MODELED LIMB

The radius of the limbs varies within the population [40]. In Fig. 12 the radius of the multilayered concentric cylinder was swept from 40 mm to 60 mm, while the thicknesses of the layers were scaled to preserve the proportions of Table I. The implant was placed at a depth equivalent to half of the cylinder's radius, the transverse position was zero, the longitude of the implant was 30 mm and the longitudinal position of its electrodes was 95 mm and 135 mm (i.e., centered regarding the inter-electrode region). The applied current was limited to obtain a maximum SAR of 20 W/kg ranging from 0.34 A_{rms} to 0.58 A_{rms} (Fig. 12a).

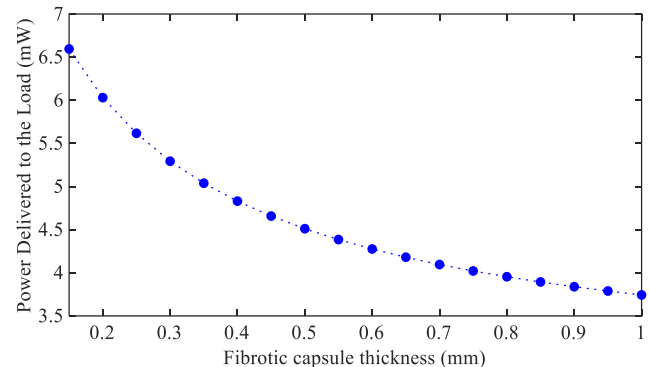


FIGURE 10. PDL as a function of the thickness of a fibrotic capsule. The fibrotic tissue conductivity was set to 0.16 S/m. The fibrotic capsule thickness increment is illustrated in the supplementary material ("S10.gif").

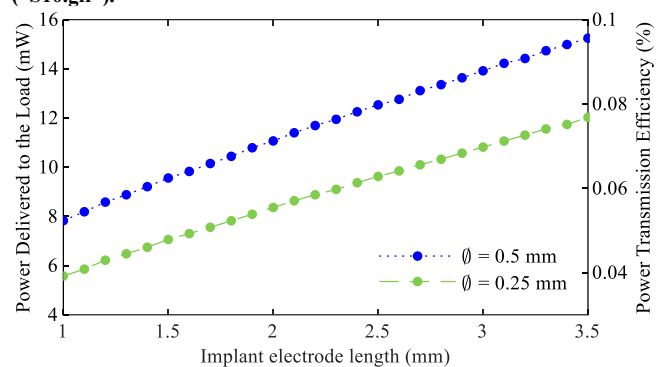


FIGURE 11. PDL and PTE as a function of the implant electrode length for two different electrode diameters: 0.5 mm and 0.25 mm.

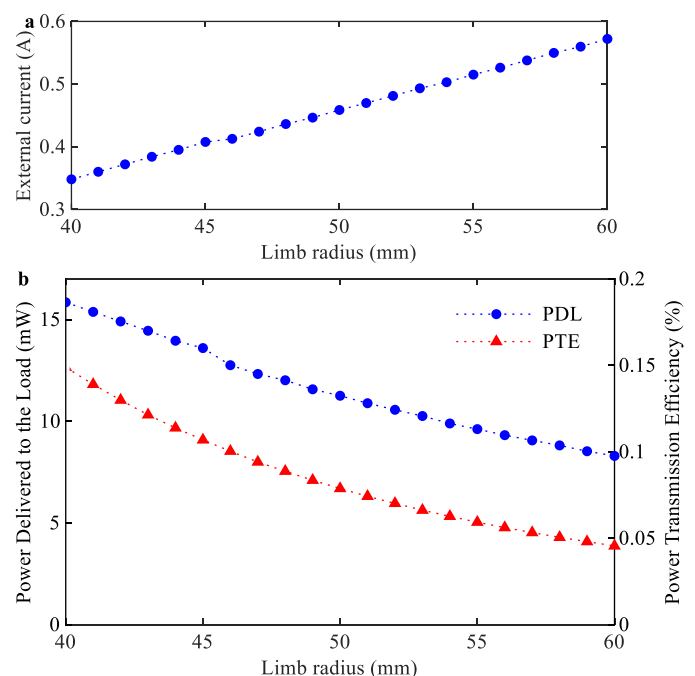


FIGURE 12. a) Maximum external current that can be applied to obtain an averaged SAR of 20 W/kg. b) PDL and PTE as a function of the radius of the limb. The thicknesses of the layers were scaled with the limb radius to preserve the proportion of Table I. The limb radius increment is illustrated in the supplementary material ("S12.gif").

The results show, that both PDL and PTE decrease as the multilayered cylinder radius increases (Fig.12b). The PDL for a radius of 60 mm is 8.3 mW (i.e., a reduction of 48% compared to the 40 mm case), and the PTE for the 60 mm case is 0.046% (i.e., a reduction of 69% compared to the 40 mm case).

V. DISCUSSION

The numerical results obtained here indicate that the proposed WPT technique based on volume conduction can be a proper method to power networks of deeply implanted AIMDs at the limbs. This claim is supported by three pieces of evidence presented here. First, powers above 10 mW can be obtained with thread-like thin and elongated implants (e.g., diameter equal to 500 μm and length 30 mm), while the externally applied currents comply with safety limitations (i.e., $\text{SAR} \leq 20 \text{ W/kg}$ for extremities, and a frequency above 5 MHz). This obtained power is orders of magnitude higher than the power required for most existing AIMDs [41]. Second, the generated electric field is coarsely uniform within the region encompassed by the external electrodes. Thus, the maximum voltage that the implants can receive is almost independent on their implantation depth; deeply implanted devices can be powered. Third, the presence of multiple implants placed just a few millimeters apart has a minor impact on their PDL, while it increases the PTE of the system.

An unanticipated and counterintuitive finding is that as the fat layer becomes thicker, the power picked up by the implant placed at the muscle tissue becomes higher. This is attributable to two main reasons. First, fat tissue is more insulating than the underlying muscle tissue and this enables safe delivery of higher currents: a thicker fat layer around the external electrodes (i.e., lower conductivity than the muscle layer) reduces the edge effect of the external electrodes, making it possible to increase the applied external current. Second, the increase in thickness of the fat layer at the expense of the muscle layer causes that more current will flow through the muscle, increasing the electric field within this layer. Therefore, the PDL of the implants increases.

In this study, for the sake of simplicity and because the waveform of the applied current does not influence the PDL (for the case where the implant load is a purely resistive load [20]) the applied external current was considered purely sinusoidal. However, by applying the external currents in the form of short bursts, the peak voltage that an implant can obtain using volume conduction can be increased. This is relevant for most electronic implants, and particularly for digital implants, as these devices will typically require a minimum voltage to operate. By delivering the ac current in the form of bursts rather than continuously, the received peak voltage can be increased without incrementing the complexity of the implant's electronics (i.e., in most of the scenarios, the implant circuit will not require bulky boost converters). Regarding the safety limitations, if the current bursts are applied with a repetition frequency F (Hz) of tens of hertz, and the burst has a duration B (s), (1) becomes

$$\text{SAR} = \frac{\sigma FB |E_{\text{peak}}|^2}{\rho} \quad (15)$$

However, it must be considered that, by delivering the current in the form of bursts rather than continuously, the field is no longer purely sinusoidal. It must be verified that the low frequency components of the modulation harmonics cannot produce undesired stimulation [42].

Another interesting result is that, even considering a capsule formation with a thickness of 1 mm around the implant electrodes (i.e., twice the diameter of the considered electrode), the implant would be able to harvest powers above 3.7 mW for the studied geometry. However, it must be mentioned that although in this study it was used a fibrotic tissue conductivity of 0.16 S/m, which is the most used in the literature [39], the electrical properties of the fibrotic tissue are not clearly determined [43], [44]. Therefore, the electrical properties and growth of the fibrotic capsule are key features to study in future long term *in vivo* studies.

In this work, the size of the implant was intentionally kept constant. This is due to the fact that the separation distance between the implant electrodes and the dimensions of the electrodes were deeply studied in [20]. Considering that the implant electrodes are part of a flexible tubing that includes the implant electronics, if the diameter of this tubing coincides with the electrodes' diameter (500 μm), the volume of the AIMDs would be 6.5 mm^3 . The small cross section of the implants combined with their thread-like shape will allow their percutaneous injection. Previous *in vivo* studies emphasized the relevance of inserting the whole implant into the target muscle [45]. Muscles experience longitudinal displacements with respect to neighboring muscles, therefore, if an implant crosses an interface between them, it will be subjected to a great mechanical stress. Additionally, due to the corrosive body environment, stress can induce chemical changes and lower the strength of the materials. To avoid these damages we are currently developing and mechanically validating new robust and resilient [46] implant encapsulations using testbeds for accelerated validation of AIMDs [47].

Table III compares the obtained results against state-of-the-art AIMDs deployed more than 3 cm deep. This comparison highlights the potential of the proposed technique to obtain high power densities (i.e., PDL per implant volume).

Regarding the external electrodes, the results show that to power deeply implanted devices (e.g., depth above 10 mm) it is preferable a separation distance considerably larger than the length of the implant assuming that the implant is placed in the central region between both external electrodes. However, if this separation distance is too large, the PTE is reduced because, as the separation distance between the external electrodes increases, more power is dissipated through the tissues, while the PDL remains almost constant. Another noteworthy observation related to the external electrodes is that wider external

Table III
COMPARISON OF AIMDS DEPLOYED MORE THAN 3 CM DEEP

	This work	Zhang [48]	Zada [49]	Meng [50]	Agrawal [51]
Technology	VC	IC	MW	US	MW
Type of study	<i>in silico</i>	<i>ex vivo</i>	<i>in vitro</i>	<i>in vitro</i>	<i>in vivo</i>
Implantation depth (mm)	30	50	45	30	42
Implant volume (mm ³)	6.7	1140	21 [‡]	1 [‡]	12
Implant section (mm ²)	0.2	900	42	1.3	1.77
PDL (mW)	11.6	1.5	4.7	2	0.45
PDL/Volume (mW/mm ³)	1.73	0.001	0.22 [‡]	2 [‡]	0.04

VC: Volume Conduction. IC: Inductive Coupling. MW: Microwave. US: Ultrasounds.

[‡] Only includes the volume of the energy pick-up element. The volume will be increased by attaching a functional AIMD circuitry.

electrodes allow the application of higher external electric currents, thereby increasing the PDL. The results show that for a wider electrode, Z_{ex} is reduced, and consequently, the PTE improves. Nevertheless, the width of the band electrodes is obviously limited by the available space on the limbs.

VI. CONCLUSIONS

In this study it is numerically demonstrated that the proposed WPT technique based on volume conduction can be a safe and effective method for powering electronic devices deeply implanted within human limbs. Powers above 10 mW can be obtained by thin (diameter < 1 mm) thread-like implants, which can be easily implanted using minimally invasive procedures such as percutaneous injections.

The results show that the maximum PDL and PTE are mostly related to the tissue impedance as measured across the implant electrodes (Z_{im}). The main feature that affects this impedance, apart from the implant electrode size [20], is the kind of tissue that surrounds the implant: the PDL ranges from 10.4 mW in muscle tissue to 0.4 mW in fat tissue. Other features that affect PDL and PTE are the size and location of the external electrodes. Larger external electrodes allow the application of higher external currents, increasing the PDL. Additionally, to maximize the PTE in deeply implanted devices, the external electrodes must have a separation distance moderately larger than the implant's length. The geometrical dimensions and the tissue anatomy of the limbs also contribute to the PDL and PTE. For example, having a fat layer above 10 mm significantly increases the PDL for an implant placed inside muscle tissue. Furthermore, as the diameter of the modeled limb increases, the PDL and PTE are decreased. Nevertheless, it is worth noting that transferred powers of several mW were obtained in all the cases reported here.

It must be acknowledged that although tens of milliwatts can be safely transferred using the proposed WPT technique, the PTE of this method is considerably lower compared to the PTE of focalized WPT methods (e.g., inductive coupling). However, it also must be acknowledged that the proposed WPT technique is a non-focalized method and that the implants do not interfere substantially in terms of power extraction if they are spaced few millimeters away.

Therefore, the proposed WPT technique can be particularly suitable to power distributed networks of minimally invasive implants.

REFERENCES

- [1] N. Hird, S. Ghosh, and H. Kitano, "Digital health revolution: Perfect storm or perfect opportunity for pharmaceutical R&D?," *Drug Discovery Today*. 2016. doi: 10.1016/j.drudis.2016.01.010.
- [2] K. Famm, B. Litt, K. J. Tracey, E. S. Boyden, and M. Slaoui, "Drug discovery: A jump-start for electroceuticals," *Nature*. 2013. doi: 10.1038/496159a.
- [3] W. D. Memberg *et al.*, "Implanted neuroprosthesis for restoring arm and hand function in people with high level tetraplegia," *Archives of Physical Medicine and Rehabilitation*. 2014. doi: 10.1016/j.apmr.2014.01.028.
- [4] L. P. Maneski *et al.*, "Electrical stimulation for the suppression of pathological tremor," *Medical and Biological Engineering and Computing*, 2011, doi: 10.1007/s11517-011-0803-6.
- [5] A. P. Valdunciel *et al.*, "Intramuscular stimulation of muscle afferents attains prolonged tremor reduction in essential tremor patients," *IEEE Transactions on Biomedical Engineering*, p. 1, 2020, doi: 10.1109/TBME.2020.3015572.
- [6] C. Rodrigues *et al.*, "Comparison of Intramuscular and Surface Electromyography Recordings Towards the Control of Wearable Robots for Incomplete Spinal Cord Injury Rehabilitation," in *2020 8th IEEE RAS/EMBS International Conference for Biomedical Robotics and Biomechatronics (BioRob)*, 2020, pp. 564–569. doi: 10.1109/BioRob49111.2020.9224361.
- [7] I. Bioelectronics, K. Agarwal, S. Member, and R. Jegadeesan, "Wireless Power Transfer Strategies for Implantable Bioelectronics," *IEEE Reviews in Biomedical Engineering*, vol. 10, pp. 136–161, 2017.
- [8] A. K. RamRakhyani, S. Mirabbasi, and M. Chiao, "Design and optimization of resonance-based efficient wireless power delivery systems for biomedical implants," *IEEE Transactions on Biomedical Circuits and Systems*, vol. 5, no. 1, pp. 48–63, 2011, doi: 10.1109/TBCAS.2010.2072782.
- [9] M. Kiani, U. M. Jow, and M. Ghovanloo, "Design and optimization of a 3-coil inductive link for efficient wireless power transmission," *IEEE Transactions on Biomedical Circuits and Systems*, vol. 5, no. 6, pp. 579–591, 2011, doi: 10.1109/TBCAS.2011.2158431.
- [10] J. S. Ho *et al.*, "Wireless power transfer to deep-tissue microimplants," *Proceedings of the National Academy of Sciences of the United States of*

- America*, vol. 111, no. 22, pp. 7974–9, 2014, doi: 10.1073/pnas.1403002111.
- [11] M. Meng and M. Kiani, “Design and Optimization of Ultrasonic Wireless Power Transmission Links for Millimeter-Sized Biomedical Implants,” *IEEE Transactions on Biomedical Circuits and Systems*, 2017, doi: 10.1109/TBCAS.2016.2583783.
- [12] A. Ibrahim, M. Meng, and M. Kiani, “A Comprehensive Comparative Study on Inductive and Ultrasonic Wireless Power Transmission to Biomedical Implants,” *IEEE Sensors Journal*, vol. 18, no. 9, pp. 3813–3826, 2018, doi: 10.1109/JSEN.2018.2812420.
- [13] S. Ozeri and D. Shmilovitz, “Ultrasonic transcutaneous energy transfer for powering implanted devices,” *Ultrasonics*, vol. 50, no. 6, pp. 556–566, 2010, doi: 10.1016/j.ultras.2009.11.004.
- [14] K. Fotopoulou and B. W. Flynn, “Wireless power transfer in loosely coupled links: Coil misalignment model,” *IEEE Transactions on Magnetics*, 2011, doi: 10.1109/TMAG.2010.2093534.
- [15] M. Machnoor, E. S. Gamez Rodriguez, P. Kosta, J. Stang, and G. Lazzi, “Analysis and design of a 3-coil wireless power transmission system for biomedical applications,” *IEEE Transactions on Antennas and Propagation*, vol. 67, no. 8, pp. 5012–5024, 2019, doi: 10.1109/TAP.2018.2883687.
- [16] S. A. Mirbozorgi, P. Yeon, and M. Ghovanloo, “Robust Wireless Power Transmission to mm-Sized Free-Floating Distributed Implants,” *IEEE Transactions on Biomedical Circuits and Systems*, vol. 11, no. 3, pp. 692–702, 2017, doi: 10.1109/TBCAS.2017.2663358.
- [17] F. Mazzilli, C. Lafon, and C. Dehollain, “A 10.5 cm ultrasound link for deep implanted medical devices,” *IEEE Transactions on Biomedical Circuits and Systems*, vol. 8, no. 5, pp. 738–750, 2014, doi: 10.1109/TBCAS.2013.2295403.
- [18] L. Becerra-Fajardo, M. Schmidbauer, and A. Ivorra, “Demonstration of 2 mm Thick Microcontrolled Injectable Stimulators Based on Rectification of High Frequency Current Bursts,” *IEEE Transactions on Neural Systems and Rehabilitation Engineering*, vol. 25, no. 8, pp. 1343–1352, 2017, doi: 10.1109/TNSRE.2016.2623483.
- [19] L. Becerra-Fajardo, M. Tudela-Pi, and A. Ivorra, “Two-Port Networks to Model Galvanic Coupling for Intrabody Communications and Power Transfer to Implants,” *2018 IEEE Biomedical Circuits and Systems Conference (BioCAS)*, pp. 1–4, Oct. 2018, doi: 10.1109/BIOCAS.2018.8584691.
- [20] M. Tudela-Pi, L. Becerra-Fajardo, A. Garcia-Moreno, J. Minguillon, and A. Ivorra, “Power Transfer by Volume Conduction: In Vitro Validated Analytical Models Predict DC Powers above 1 mW in Injectable Implants,” *IEEE Access*, 2020, doi: 10.1109/ACCESS.2020.2975597.
- [21] J. Minguillon *et al.*, “Powering electronic implants by high frequency volume conduction: in human validation,” *bioRxiv*, p. 2021.03.15.435404, Jan. 2021, doi: 10.1101/2021.03.15.435404.
- [22] X. Hu, A. Chen, Y. Luo, C. Zhang, and E. Zhang, “Steerable catheters for minimally invasive surgery: a review and future directions,” *Computer Assisted Surgery*, vol. 23, no. 1. Taylor and Francis Ltd., pp. 21–41, Jan. 01, 2018, doi: 10.1080/24699322.2018.1526972.
- [23] M. S. Wegmueller *et al.*, “An Attempt to Model the Human Body as a Communication Channel,” *IEEE Transactions on Biomedical Engineering*, vol. 54, no. 11, pp. 2057–2063, 2007, doi: 10.1109/TBME.2007.895111.
- [24] M. A. Callejon, J. Reina-Tosina, D. Naranjo-Hernandez, and L. M. Roa, “Galvanic coupling transmission in intrabody communication: A finite element approach,” *IEEE Transactions on Biomedical Engineering*, 2014, doi: 10.1109/TBME.2013.2289946.
- [25] B. Kibret, M. H. Seyedi, D. T. H. Lai, and M. Faulkner, “Investigation of galvanic-coupled intrabody communication using the human body circuit model,” *IEEE Journal of Biomedical and Health Informatics*, vol. 18, no. 4, pp. 1196–1206, 2014, doi: 10.1109/JBHI.2014.2301165.
- [26] IEEE, *IEEE Standard for Safety Levels With Respect to Human Exposure to Radio Frequency Electromagnetic Fields, 3 kHz to 300 GHz*. 2019.
- [27] International Commission on Non-Ionizing Radiation Protection, “Guidelines for limiting exposure to electromagnetic fields (100 kHz to 300 GHz),” *Health Physics*, vol. 118, no. 5, pp. 483–524, 2020, doi: 10.1097/HP.0000000000001210.
- [28] A. Vander Vorst, A. Rosen, and Y. Kotsuka, *RF/Microwave Interaction with Biological Tissues*. New Jersey: John Wiley & Sons, Inc., 2006.
- [29] M. A. Callejon, J. Reina-Tosina, D. Naranjo-Hernandez, and L. M. Roa, “Galvanic coupling transmission in intrabody communication: A finite element approach,” *IEEE Transactions on Biomedical Engineering*, vol. 61, no. 3, pp. 775–783, 2014, doi: 10.1109/TBME.2013.2289946.
- [30] S. Grimnes and Ø. G. Martinsen, “Passive Tissue Electrical Properties,” in *Bioimpedance and Bioelectricity Basics*, 3 rd., Elsevier Ltd, 2015, pp. 77–118. doi: 10.1016/B978-0-12-374004-5.X0001-3.
- [31] D. Andreuccetti, R. Fossi, and C. Petrucci, “An Internet resource for the calculation of the dielectric properties of body tissues in the frequency range 10 Hz - 100 GHz,” *IFAC-CNR, Florence (Italy)*, 1997.
- [32] P. Hasgall *et al.*, “IT’IS Database for thermal and electromagnetic parameters of biological tissues, Version 4.0,” *IT’IS*, 2018.

- [33] M. Brian S., *An introduction to materials engineering and science for chemical and materials engineers*. 2004. doi: 10.5860/choice.41-5327.
- [34] L. Becerra-Fajardo, M. Tudela-Pi, and A. Ivorra, "Two-Port Networks to Model Galvanic Coupling for Intrabody Communications and Power Transfer to Implants," *2018 IEEE Biomedical Circuits and Systems Conference (BioCAS)*, pp. 1–4, 2018, doi: 10.1109/BIOCAS.2018.8584691.
- [35] W. H. Hayt, J. Kemmerly, and S. M. Durbin, "Two-port networks," in *Engineering Circuit Analysis*, 8th ed., New York: McGraw-Hill, 2012, pp. 687–732.
- [36] IEC/IEEE International, "Determining the peak spatial-average specific absorption rate (SAR) in the human body from wireless communications devices, 30 MHz to 6 GHz - Part 1: General requirements for using the finite-difference time-domain (FDTD) method for SAR calculations," *IEC/IEEE 62704-1*, pp. 1–86, 2017, doi: 10.1109/IEEESTD.2017.8088404.
- [37] H. Kanehisa, M. Miyatani, K. Azuma, S. Kuno, and T. Fukunaga, "Influences of age and sex on abdominal muscle and subcutaneous fat thickness," *European Journal of Applied Physiology*, 2004, doi: 10.1007/s00421-003-1034-9.
- [38] W. Murphy, J. Black, and G. Hastings, *Handbook of biomaterial properties*, 2 nd. New York: Springer Science, 2016. doi: 10.1007/978-1-4939-3305-1.
- [39] W. M. Grill and J. Thomas Mortimer, "Electrical properties of implant encapsulation tissue," *Annals of Biomedical Engineering*, 1994, doi: 10.1007/BF02368219.
- [40] N. Benítez Brito *et al.*, "Relationship between mid-upper arm circumference and body mass index in inpatients," *PLoS ONE*, 2016, doi: 10.1371/journal.pone.0160480.
- [41] J. S. Ho *et al.*, "Wireless power transfer to deep-tissue microimplants," *Proceedings of the National Academy of Sciences of the United States of America*, 2014, doi: 10.1073/pnas.1403002111.
- [42] IEEE International Committee on Electromagnetic Safety, "IEEE Standard for Safety Levels with Respect to Human Exposure to Radio Frequency Electromagnetic Fields , 3 kHz to 300 GHz," *Inc.*, New York, NY, 2006, doi: 10.1109/IEEESTD.2006.99501.
- [43] M. M. Lowery, R. F. F. Weir, and T. A. Kuiken, "Simulation of intramuscular EMG signals detected using implantable myoelectric sensors (IMES)," *IEEE Transactions on Biomedical Engineering*, 2006, doi: 10.1109/TBME.2006.881774.
- [44] F. Suska, L. Emanuelsson, A. Johansson, P. Tengvall, and P. Thomsen, "Fibrous capsule formation around titanium and copper," *Journal of Biomedical Materials Research - Part A*, 2008, doi: 10.1002/jbm.a.31575.
- [45] A. Ivorra, L. Becerra-Fajardo, and Q. Castellví, "In vivo demonstration of injectable microstimulators based on charge-balanced rectification of epidermically applied currents," *Journal of Neural Engineering*, vol. 12, no. 6, 2015, doi: 10.1088/1741-2560/12/6/066010.
- [46] W. J. Zhang and C. A. van Luttervelt, "Toward a resilient manufacturing system," *CIRP Annals*, vol. 60, no. 1, pp. 469–472, 2011, doi: <https://doi.org/10.1016/j.cirp.2011.03.041>.
- [47] J. L. Gbur and J. J. Lewandowski, "Fatigue and fracture of wires and cables for biomedical applications," *International Materials Reviews*, vol. 61, no. 4, pp. 231–314, May 2016, doi: 10.1080/09506608.2016.1152347.
- [48] K. Zhang *et al.*, "Near-Field Wireless Power Transfer to Deep-Tissue Implants for Biomedical Applications," *IEEE Transactions on Antennas and Propagation*, vol. 68, no. 2, pp. 1098–1106, 2020, doi: 10.1109/TAP.2019.2943424.
- [49] M. Zada and H. Yoo, "A Miniaturized Triple-Band Implantable Antenna System for Bio-Telemetry Applications," *IEEE Transactions on Antennas and Propagation*, vol. 66, no. 12, pp. 7378–7382, 2018, doi: 10.1109/TAP.2018.2874681.
- [50] M. Meng and M. Kiani, "Design and Optimization of Ultrasonic Wireless Power Transmission Links for Millimeter-Sized Biomedical Implants," *IEEE Transactions on Biomedical Circuits and Systems*, vol. 11, no. 1, pp. 98–107, 2017, doi: 10.1109/TBCAS.2016.2583783.
- [51] D. R. Agrawal *et al.*, "Conformal phased surfaces for wireless powering of bioelectronic microdevices," *Nature Biomedical Engineering*, vol. 1, 2017, doi: 10.1038/s41551-017-0043.